hygiene

MDPI

Article

Unveiling the Mechanisms for *Campylobacter jejuni* Biofilm Formation Using a Stochastic Mathematical Model

Paulina A. Dzianach [1,2,3], **Gary A. Dykes** [3,4], **Norval J. C. Strachan** [1], **Ken J. Forbes** [5] and **Francisco J. Pérez-Reche** [1,*]

[1] School of Natural and Computing Sciences, University of Aberdeen, Aberdeen AB24 3UE, UK; paulina.dzianach@telethonkids.org.au (P.A.D.); n.strachan@abdn.ac.uk (N.J.C.S.)
[2] Child Health Analytics, Telethon Kids Institute, Nedlands, WA 6009, Australia
[3] School of Public Health, Curtin University, Perth, WA 6845, Australia; gad@uq.edu.au
[4] School of Agriculture and Food Sciences, University of Queensland, St. Lucia, QLD 4072, Australia
[5] School of Medicine, Medical Sciences and Nutrition, University of Aberdeen, Aberdeen AB24 3UE, UK; k.forbes@abdn.ac.uk
* Correspondence: fperez-reche@abdn.ac.uk

Abstract: *Campylobacter jejuni* plays a significant role in human health, food production, and veterinary practice. Biofilm formation is a likely mechanism explaining the survival of *C. jejuni* in seemingly unfavourable environments, but the underlying mechanisms are poorly understood. We propose a mathematical model to unify various observations regarding *C. jejuni* biofilm formation. Specifically, we present a cellular automaton with stochastic dynamics that describes both the probability of biofilm initiation and its subsequent growth. Our model incorporates fundamental processes such as cell rearrangement, diffusion of chemical compounds, accumulation of extracellular material, cell growth, lysis, and deactivation due to nutrient scarcity. The model predicts an optimal nutrient concentration that enhances population survival, revealing a trade-off where higher nutrient levels may harm individual cells but benefit the overall population. Our results suggest that the lower biofilm accumulation observed experimentally in aerobic conditions compared to microaerobic conditions may be due to a reduced surface invasion probability of individual cells. However, cells that do manage to invade can generate microcolonies of a similar size under both aerobic and microaerobic conditions. These findings provide new insights into the survival probability and size of *C. jejuni* biofilms, suggesting potential targets for controlling its biofilm formation in various environments.

Keywords: biofilms; extracellular matrix (ECM); cellular automata (CA); individual based modelling (IbM); *Campylobacter jejuni*

check for updates

Citation: Dzianach, P.A.; Dykes, G.A.; Strachan, N.J.C.; Forbes, K.J.; Pérez-Reche, F.J. Unveiling the Mechanisms for *Campylobacter jejuni* Biofilm Formation Using a Stochastic Mathematical Model. *Hygiene* **2024**, *4*, 326–345. https://doi.org/10.3390/hygiene4030026

Academic Editors: Luís Cardoso, Paula Oliveira and Ana Cláudia Coelho

Received: 9 July 2024
Revised: 31 July 2024
Accepted: 1 August 2024
Published: 8 August 2024

1. Introduction

Bacterial populations may exist in two main forms: a planktonic state, where individual cells live independently in a liquid medium, or as biofilms, which are densely packed bacterial communities surrounded by extracellular material [1–5]. It is important to analyse biofilm communities separately from planktonic cultures, as the behaviour of cells in biofilms differ substantially from that in planktonic cultures [2,3,5]. The emergent properties of biofilm communities allow them to survive in environments that would be too hostile for survival in a planktonic state [3,5].

For instance, biofilms have been shown to enhance the resistance of bacteria to antimicrobial treatments through various mechanisms, including the physical barrier imposed by the extracellular matrix, an altered microenvironment that makes cells less susceptible to antimicrobials, and genetic changes induced by horizontal gene transfer that spread resistance traits throughout the biofilm community [3,6–8]. Biofilms can form in various environments, such as water bodies [5,9], porous media [10], and medical devices [5,11].

Their resilience to standard disinfection methods poses significant challenges across multiple sectors, including healthcare (e.g., wounds infected by biofilms [12]), veterinary settings (e.g., biofilms in medical equipment [11]), the food industry (e.g., biofilms in food processing equipment [13,14]) and water systems (e.g., biofilms in cooling water systems [9]). Understanding the mechanisms of biofilm formation and resistance is therefore critical for developing effective disinfection and sterilization methods in these sectors.

The mathematical modelling of biofilms has been developing for many years to complement and enhance the understanding gained from empirical research [15,16]. Most models focus on estimates of the morphology of biofilms without estimating the chances of biofilm formation. Even though stochasticity has been included to various extents in biofilm modelling [17–22], both modelling and experimental approaches generally focus on biofilms in the invasive mode, i.e., when the probability that the biofilm forms is high. Although in the biofilm modelling literature it is usually acknowledged that biological systems are often governed by stochastic dynamics, the probability of a successful surface invasion has not so far received much attention. Addressing this issue may be of particular importance for biofilm-forming bacterial foodborne pathogens [14] such as *Listeria monocytogenes*, *Escherichia coli*, *Salmonella enterica*, and *Campylobacter jejuni*, whose infections are random processes described by dose–response models for the probability of infection [23–29].

Campylobacter jejuni is a particularly interesting case of a biofilm-forming bacterial pathogen. *C. jejuni* is the most common bacterial cause of gastroenteritis globally [30,31]. Despite its requirements for a low-oxygen environment, a narrow temperature range, and specialized media [32,33], *C. jejuni* remains a highly successful pathogen [34,35]. The most common way of exposure to *C. jejuni* is through the consumption of contaminated food [35], particularly undercooked poultry [36–38] and unpasteurized milk [39], or exposure to contaminated water [40,41]. This pathogen can be found in multiple locations, including farms, where it resides in the intestinal tracts of livestock and poultry, and veterinary clinics, where it can persist on surfaces and equipment [42,43]. Biofilm formation [44] and attachment to existing biofilms of *Pseudomonas aeruginosa* [45] have been identified as key factors that contribute to the survival of *C. jejuni* in environments with suboptimal growth conditions. Although various models for *C. jejuni* have been proposed [46–55], no attempt has been made to study *C. jejuni* biofilm formation through mathematical modelling.

In this paper, we describe a mathematical model that unifies various observations regarding *C. jejuni* biofilm formation. Firstly, *C. jejuni* has been reported to exhibit higher biofilm formation in low-nutrient media (MHB) compared to nutrient-rich media (Brucella broth, Bolton broth) [56,57]. Despite being highly sensitive to atmospheric oxygen concentrations, it was found that biofilms formed in food-chain-relevant aerobic conditions can in some cases be denser than those achieved in microaerobic conditions [58]. This appears to contradict findings [59] that aerobic conditions enhance the bacterial lysis of *C. jejuni*, which would presumably reduce biofilm formation. However, the same study found that starvation conditions significantly inhibit lysis [59]. This suggests a complex interplay between oxygen levels, lysis, and starvation conditions that must be considered to fully understand the success of *C. jejuni* biofilms.

The biofilm formation model reported here is based on existing mathematical models [18,60–66]. Our model accounts for fundamental processes such as the rearrangement of cells within the biofilm, diffusion of chemical compounds outside and inside of the biofilm, cell growth, lysis, and deactivation due to insufficient nutrient resources. We consider the biofilm formation process as a biological invasion, which is inherently stochastic [17,66,67], and can occur with a certain probability, depending on the conditions the cells are subjected to. This description is reminiscent of models for the spread of infections by biological invasions [67–69]. We note that there are many complex mechanisms involved in biofilm formation [15,16], which were not included in this model, e.g., quorum sensing, mixed species interactions, or the attachment of cells to an existing biofilm from the planktonic state.

Despite the specific application to *C. jejuni* presented here, the model is relevant beyond *C. jejuni* and can be adapted to include characteristics pertinent to other species, allowing for their study within a stochastic individual-based framework.

2. Model Description

Biofilm formation is simulated in a two-dimensional environment with $L \times H$ patches of linear length δ arranged on a square lattice (Figure 1). Although biofilms naturally develop in three-dimensional situations, two-dimensional simulations were used for convenience in terms of numerical simulations and the visualization of the data. This approach allows us to efficiently capture key dynamics and interactions within the biofilm, providing valuable insights while maintaining computational tractability. Computational efficiency is crucial for running multiple stochastic realisations for a given set of parameters, enabling a statistical understanding of the model predictions.

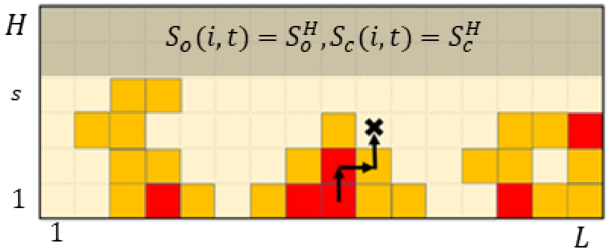

Figure 1. Geometry of the space used to simulate the biofilm. The system consists of $L \times M$ patches with coordinates $x \in [1, L]$ and $y \in [1, H]$. The biofilm growth is initiated by a randomly placed cell in the bottom row with $y = 1$. Red patches represent live cells, while orange patches represent the extracellular matrix (ECM). Constant concentrations of oxygen (S_o^H) and carbon (S_c^H) are supplied at the top layer of the system. The chemical concentrations in the uncolonized layers are assumed to be equal to those supplied at the top (as indicated by the shaded patches where $S_o(i,t) = S_o^H$ and $S_c(i,t) = S_c^H$ for oxygen and carbon, respectively). A directed random path is illustrated, with the end of the path marked by a cross. The start of the path indicates where cell division has occurred, necessitating the redistribution of biofilm material to accommodate the new cell. In this example, no empty sites are encountered along the path, so the shoving algorithm terminates at the end of the path.

The sites at the bottom of the lattice represent the solid surface on which the biofilm growth can initiate. The remaining sites represent the space above the solid surface where the biofilm can grow. Each patch in this region represents an area of space that can be occupied by fluid (F), a cell (C), or ECM (E). The state of the i-th patch at time t is given by a variable $\sigma(i,t)$ that can take values F, C, or E. The neighbourhood of a patch i is denoted as $\mathcal{N}(i)$. All boundaries are assumed to be closed such that a patch i has $|\mathcal{N}(i)|$ neighbours: four if it is in the interior, three if it is along an edge, and two if it is at a corner.

Two types of chemical compounds are considered: a carbon source and oxygen with concentration fields $S_c(i,t)$ and $S_o(i,t)$, respectively. In the case of *C. jejuni,* the carbon source represents growth limiting compounds such as amino acids [70]. Since *C. jejuni* is a microaerophilic organism, it requires oxygen to grow, but small concentrations are optimal for cell survival. Indeed, it was observed that high oxygen concentrations promote bacterial lysis [59].

The system dynamics involve vital cell transitions (duplication, lysis, or deactivation) and substrate rearrangements associated with cell nutrient consumption and diffusion. We assume that concentration changes in the substrate are fast compared to vital dynamics events. Under this assumption, the system dynamics can be implemented as a sequential algorithm in which vital dynamic events are followed by fast substrate rearrangement, as shown in Figure 2.

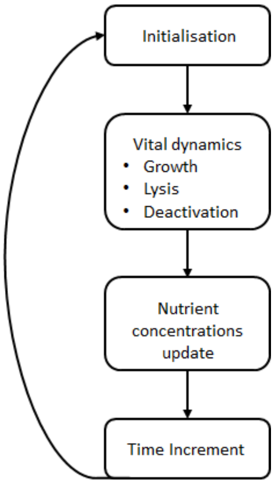

Figure 2. Schematic diagram of the biofilm model simulation algorithm.

We assume that the duplication (i.e., growth), lysis, or deactivation of a cell at patch i can occur randomly with transition rates $\lambda_g(i,t)$, $\lambda_l(i,t)$, and $\lambda_d(i,t)$, respectively. Such rates depend on the substrate concentration fields $S_c(i,t)$ and $S_o(i,t)$ as described below.

Transitions in the state of cells are simulated as random events in continuous time using a kinetic Monte Carlo algorithm (also known as n-fold way or Gillespie algorithm) [71]. This algorithm allows the time increment Δt between consecutive events to be efficiently obtained through the formulation of a Poisson process (see Appendix A).

To gain statistical insight on biofilm formation, we simulated 100 stochastic realisations for each pair (S_c^H, S_o^H), starting from a randomly placed cell at the bottom of the system (layer with $y = 1$ in Figure 1).

We now describe in more detail the implementation of the vital cell transitions and substrate compound dynamics. The model parameters are listed in Table 1. Where possible, parameter values were sourced from the literature. For parameters not directly available from the literature or those dependent on model approximations (e.g., diffusion constants), appropriate values were assigned.

2.1. Cell Growth

Growth occurs through the duplication of cells. If a cell in patch i duplicates, the offspring is placed at a randomly chosen site j in the neighbourhood $\mathcal{N}(i)$ of patch i:

$$C(i,t) \overset{\lambda_g(i,t)}{\rightarrow} C(i,t+\Delta t) + C(j,t+\Delta t). \tag{1}$$

Only for cases when one of the sites in $\mathcal{N}(i)$ are in the fluid state, the offspring is randomly placed in one of these sites. In contrast, if all sites in $\mathcal{N}(i)$ are occupied by the cells or ECM, a random directed path (see Appendix B) is applied to redistribute the biofilm mass, which is defined as the set of patches occupied by the cells or ECM.

We assume that growth is promoted by the carbon source concentration $S_c(i,t)$. The growth rate $\lambda_g(i,t)$ of a cell at site i and time t is given by the following:

$$\lambda_g(i,t) = r_g \frac{S_c(i,t)}{S_c(i,t) + K_g}. \tag{2}$$

Equation (2) represents a standard Monod growth curve, governed by the local growth limiting nutrient concentration $S_c(i,t)$ with a maximum specific growth rate r_g and Monod growth half saturation coefficient K_g.

The blue dashed curve in Figure 3 illustrates how the growth rate increases with increasing nutrient concentration and asymptotically approaches the maximum value, r_g.

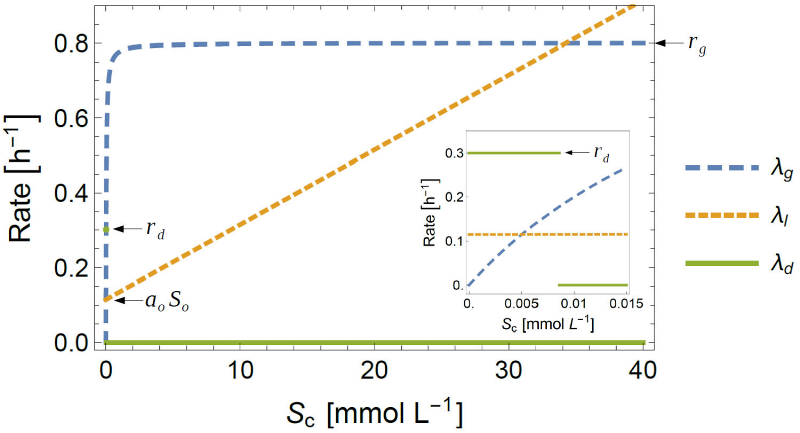

Figure 3. Effect of concentration of growth limiting compound Sc on the rates of growth, λ_g, lysis, λ_l, and deactivation, λ_d, for $S_o = 0.05$ mmol L^{-1} and parameters given in Table 1. The inset shows the dependence of the rates on the nutrient concentration for the model parameters in Table 1.

2.2. Cell Lysis

Whenever lysis occurs at site i, the living cell at this site is removed from the system and replaced by ECM material:

$$C(i,t) \quad \overset{\lambda_l(i,t)}{\rightarrow} \quad E(i,t+\Delta t). \tag{3}$$

This simulates the bursting of the cell membrane and release of the cell material into the biofilm matrix. Since both starvation conditions and enhanced oxygen conditions were found experimentally to significantly impact the measured lysis capacity of *C. jejuni* [59], we take both compounds into account in the lysis rate of the model. In particular, we assume a simple linear relation between the substrate concentrations and the lysis rate:

$$\lambda_l(i,t) = a_c S_c(i,t) + a_o S_o(i,t). \tag{4}$$

Here, $a_c, a_o \geq 0$ quantify the effect of concentration of chemical compounds on the lysis rate. Figure 3 illustrates the increase in the lysis rate of a cell as the nutrient concentration increases at the patch occupied by the cell.

2.3. Cell Deactivation

Deactivation occurs when the uptake rate of the growth-limiting compound falls below a certain threshold value. In a deactivation event, a live cell is removed from the system in a similar way to a lysis event. Unlike a lysis event, however, no extracellular material is released through deactivation. This simulates the cell simply “shutting down” or entering a coccoid, viable but non-culturable (VBNC) state of minimal metabolic activity. Although theoretically, cells may be resuscitated from the VBNC state, this process is poorly understood and the likelihood is very low; hence, in this model, the deactivation process is irreversible [72]. The deactivation rate is implemented as follows:

$$\lambda_d(i,t) = r_d \Theta(u_{min} - u_c(i,t)), \tag{5}$$

where $\Theta(x)$ is the Heaviside step function, whose value is zero for $x < 0$ and one for $x > 0$. The quantity $u_c(i,t)$ is the uptake rate of compound S_c, implemented in the model by a Monod equation with an intrinsic maximum uptake rate, U_c^{max}, and a half saturation constant K_c: $u_c(i,t) = U_c^{max} S_c(i,t)/(S_c(i,t) + K_c)$. According to Equation (5), deactivation can only occur when the uptake rate is below a minimum value u_{min}. Accordingly, deactivation is restricted to values of the nutrient concentration below a threshold, i.e., for $S_c < S_c^d = K_c u_{min}(U_c^{max} - u_{min})^{-1}$. Figure 3 illustrates the dependence of $\lambda_d(i,t)$ on $S_c(i,t)$ for the values of the parameters u_{min}, U_c^{max}, and K_c given in Table 1.

2.4. Substrate Compounds Dynamics

Changes in the concentrations of chemical compounds (i.e., oxygen and the nutrient source) occur in our model through their uptake by live cells and diffusion. The diffusion process in our model is governed by a modified Fick's second law, with changes introduced to include the influence of nutrient uptake by bacteria on chemical concentrations and the differences in the diffusion coefficient at different stages of biofilm development [61]. The latter modification has been introduced to account for the heterogeneity of the biofilm structure, which resembles a porous material [64,65]. Diffusion in porous media is a well-known example of anomalous (non-Fickian) diffusion, in which the quadratic displacement of molecules is not proportional to time [65]. Instead, anomalous diffusion corresponds to a time-dependent diffusion coefficient, $D(t)$ [65]. Introducing a density-dependent diffusion coefficient has been previously applied to mathematical models of biofilms [64]. In our model, the diffusion coefficient at time t is given by the following equation:

$$D(t) = \rho_{\mathrm{B}}(t)D_{\mathrm{B}} + (1 - \rho_{\mathrm{B}}(t))D_{\mathrm{F}}. \tag{6}$$

In Equation (6), D_{B} represents an effective diffusion constant through biofilm mass (i.e., when patch i is occupied by a cell or ECM) and D_{F} represents the diffusion constant in the fluid. The quantity $\rho_{\mathrm{B}}(t)$ is the density of the biofilm and it is calculated as a dimensionless ratio as follows:

$$\rho_{\mathrm{B}}(t) = \frac{\text{No. of patches occupied by biomass}}{\text{No. of patches occupied by biomass } + \text{ No. pores}}, \tag{7}$$

where

$$\text{No. of patches occupied by biomass} = \sum_{i=1}^{L \cdot H} \begin{cases} 1, & \sigma(i,t) = C \\ 1 - \frac{n_{\mathrm{E}}(i,t)}{N_{\mathrm{E}}}, & \sigma(i,t) = E \\ 0 & \sigma(i,t) = F \end{cases}. \tag{8}$$

When patch i is occupied by the ECM and the ECM uptake mechanism is active, $n_{\mathrm{E}}(i,t)$ gives the number of times that part of the ECM has been consumed at site i by cells in $\mathcal{N}(i)$. The pores are defined as sites for which $\sigma(i,t) = F$, which are contained within the biofilm, i.e., no path can be drawn from the site to the biofilm boundary layer without crossing a site which is occupied by biomass. Note that if there is no biomass present, $D(t) = D_{\mathrm{F}}$. In contrast, if the biofilm is fully compact, $D(t) = D_{\mathrm{B}}$.

The change in compound k (carbon or oxygen) concentration at site i with time is given by the following:

$$\frac{\partial S_k(i,t)}{\partial t} = D(t)\nabla^2 S_k(i,t) - u_k(i,t). \tag{9}$$

Here, $k = \mathrm{c}, \mathrm{o}$ for carbon and oxygen substrates, respectively, and

$$u_k(i,t) = \begin{cases} U_k^{\max} \frac{S_k(i,t)}{S_k(i,t) + K_k}, & \text{if } \sigma(i,t) = C \\ 0, & \text{otherwise} \end{cases}, \tag{10}$$

is the uptake of the k-th chemical compound at patch i if it is occupied by a cell at time t.

Similar to previous models for biofilm formation [61,63], we assume that diffusion and nutrient uptake occur much faster than vital cell transitions. Specifically, we assume that immediately after a change in biofilm geometry or composition—due to cell division, deactivation, or lysis—chemical compounds reach a quasi-steady state. The substrate concentrations are then assumed to remain constant until the next cell transition event, at which point they reach a new quasi-steady state.

While this assumption simplifies the real dynamics of substrates, which may not always reach a quasi-steady state between consecutive cell transitions, it is addressed in our simulations by using effective diffusion coefficients (Table 1). These coefficients are smaller than those expected in realistic settings [73]. The idea is that the concentrations achieved in a quasi-steady state with a smaller diffusion coefficient approximate the concentrations reached before a quasi-steady state is fully established with a larger coefficient.

In the quasi-steady regime, $\frac{\partial S_k(i,t)}{\partial t} = 0$, and Equation (9) reduces to a Poisson equation,

$$\nabla^2 S_k(i,t) = \frac{u_k(i,t)}{D(t)}, \tag{11}$$

which was solved numerically using the finite difference method [74], imposing closed boundary conditions at all boundaries with constant substrate concentrations for all patches in rows with $y > s$ that have not been colonized yet (cf. shaded upper layers in Figure 1). With these assumptions, the concentration fields are given by the following equations:

$$\sum_{j \in \mathcal{N}(i)} S_k(j,t) - |\mathcal{N}(i)| S_k(i,t) = \frac{\delta^2}{D} \begin{cases} u_k(i,t), & i \le s \cdot L \\ S_k^{\mathrm{H}}, & i > s \cdot L \end{cases}, \quad i = 1,2,\ldots,L, \;\; k = \mathrm{c},\mathrm{o} \tag{12}$$

These equations can be expressed in matrix form and numerically solved for $S_k(i,t)$.

Table 1. Parameter values used in our simulations and corresponding references motivating the choice of the parameter values.

Parameter	Description	Value(s)	Unit	Reference
D_{B}	Effective diffusion coefficient of the chemical compounds in the biofilm matrix	9×10^{-11} and 9×10^{-10}	$\mathrm{m}^2\,\mathrm{h}^{-1}$	Calibrated ourselves through numerous simulations to produce conditions in which biofilm development would affect chemical concentrations for given parameters.
D_{F}	Effective diffusion coefficient of the chemical compounds in liquid	9×10^{-10}	$\mathrm{m}^2\,\mathrm{h}^{-1}$	As above.
$U_{\mathrm{o}}^{\max}$	Maximum uptake rate of oxygen	4.5×10^{-10}	$\mathrm{mmol}\,\mathrm{h}^{-1}$	Order of magnitude obtained from oxidation rates of *C. jejuni* [75].
K_{o}	Monod coefficient for oxygen uptake rate	3×10^{-3}	$\mathrm{mmol}\,\mathrm{L}^{-1}$	Based on saturation constant estimates for *C. jejuni* in regards to changes in dissolved oxygen concentrations [75].
$U_{\mathrm{c}}^{\max}$	Maximum uptake rate of the carbon source	4.5×10^{-9}	$\mathrm{mmol}\,\mathrm{h}^{-1}$	We assumed it to be 10 times larger than maximum oxygen uptake, due to higher need to utilize the carbon source.
K_{c}	Monod coefficient for growth limiting compound uptake	0.03	$\mathrm{mmol}\,\mathrm{L}^{-1}$	Assumed 10 times larger than K_{o} due to higher need to utilize the carbon source.
r_{g}	Maximum division rate of *C. jejuni*	0.8	h^{-1}	Maximum growth rate of *C. jejuni* 104 at 42 °C, in BHI medium [76].
K_{g}	Monod coefficient for growth	0.03	$\mathrm{mmol}\,\mathrm{L}^{-1}$	Assumed to be equal to K_{c}, due to the growth-limiting nature of S_{c} and previously found direct proportionality of growth rate and substrate uptake for *E. coli* [77].
r_{d}	Deactivation rate	0.3	h^{-1}	Approximate death rate of *C. jejuni* in water at 37 °C in stationary conditions [78].
$u_{\min}$	Minimum uptake rate of S_{c}	1×10^{-9}	$\mathrm{mmol}\,\mathrm{h}^{-1}$	Assumed to be lower but have the same order of magnitude as the maximum uptake rate of the carbon source $U_{\mathrm{c}}^{\max}$.
a_{c}	Lysis coefficient for carbon source concentration	0.02	$\mathrm{L}\,\mathrm{mmol}^{-1}\,\mathrm{h}^{-1}$	Approximated to produce a slightly higher lysis rate value in aerobic conditions than the maximum growth rate (~0.85 h^{-1}), and a slightly lower lysis rate value in microaerobic conditions (~0.69 h^{-1}) for $S_{\mathrm{c}}^{\mathrm{H}} = 13\ \mathrm{mmol}\,\mathrm{h}^{-1}$.
a_{o}	Lysis coefficient for oxygen concentration	2.3	$\mathrm{L}\,\mathrm{mmol}^{-1}\,\mathrm{h}^{-1}$	As above.

3. Results and Discussion

3.1. Behaviour of a Single Cell for Given Chemical Concentrations

Before studying the predicted behaviour of a population of cells forming a biofilm, it is instructive to study the behaviour of a single cell depending on the chemical concentrations $S_c(i,t)$ and $S_o(i,t)$ at the patch i occupied by the cell. In particular, we consider the probability $P_g(i,t)$ that growth occurs before lysis or deactivation. This can be expressed in terms of the rates for growth, lysis, and deactivation as follows:

$$P_g(i,t) = \frac{\lambda_g(i,t)}{\lambda_g(i,t) + \lambda_l(i,t) + \lambda_d(i,t)}. \tag{13}$$

The dependence of P_g on the chemical concentrations at the patch can be obtained by using the dependence of the rates on the chemical concentrations given by Equation (2), (4), and (5). The colour map in Figure 4 shows the probability P_g for a cell as a function of chemical concentrations S_c and S_o in the patch occupied by the cell for the model parameters given in Table 1. The chemical concentration space (S_c, S_o) can be naturally split into two regions separated by a threshold line where $P_g = \frac{1}{2}$. We shall refer to this line as the growth likelihood threshold (in a probabilistic sense). Below the line, the growth probability is $P_g > \frac{1}{2}$ so that growth is more likely than deactivation and lysis. In contrast, $P_g < \frac{1}{2}$ above the line, and growth is less likely than deactivation or lysis. One can show that $P_g = \frac{1}{2}$ implies that the effective rate of growth $\lambda_g - \lambda_l - \lambda_d$ becomes zero, i.e., the rate of growth is exactly balanced by the rates of no growth at the threshold line.

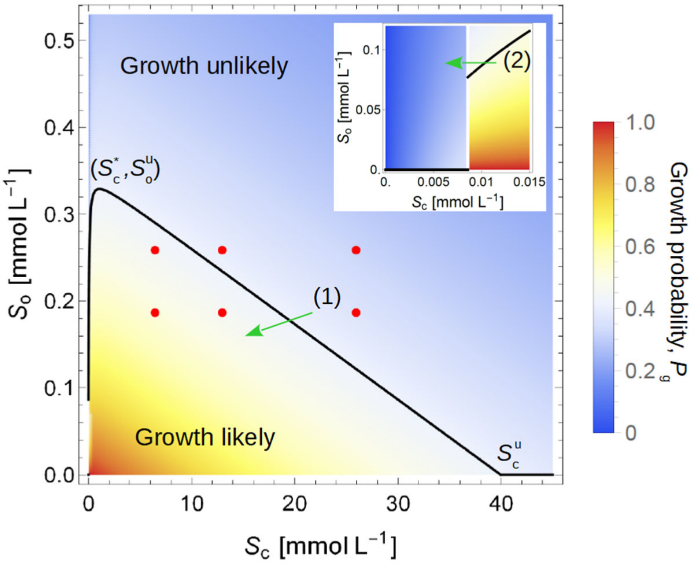

Figure 4. Colour map for the probability of growth of a cell (P_g) as a function of the nutrient and oxygen concentrations at the patch occupied by the cell. The black curve corresponding to $P_g = \frac{1}{2}$ splits the space of chemical concentrations into a region where growth is more likely than lysis or deactivation ($P_g > \frac{1}{2}$, below the curve) and a region where lysis or deactivation are more likely than growth ($P_g < \frac{1}{2}$, above the curve). The value S_c^u indicates the value of the chemical nutrient concentration above which growth is unlikely for any oxygen concentration. At the point (S_c^*, S_o^u), the nutrient concentration S_o^u is optimal in the sense that growth is favoured for the widest possible range of oxygen concentrations, i.e., for $S_o \in (0, S_o^*)$. (1) indicates a cell in a patch where growth is initially unlikely but could become favourable if biofilm develops around the patch, thus leading to a local reduction in S_c and S_o as marked by the arrow. The inset shows a magnification of the behaviour for small values of the chemical concentrations. (2) indicates a cell in a patch where growth is initially favoured, but would become unlikely, as S_c and S_o reduce locally if biofilm forms around the patch. The red circles show the values of supplied chemical compounds used in the numerical simulations presented here.

The oxygen concentration at the growth threshold is given by a function of the nutrient concentration:

$$S_{\mathrm{o}} = f_{\mathrm{th}}(S_{\mathrm{c}}) = \max\left[0, -\frac{1}{a_{\mathrm{o}}}\left(a_{\mathrm{c}}S_{\mathrm{c}} - \frac{r_{\mathrm{g}}S_{\mathrm{c}}}{K_{\mathrm{g}} + S_{\mathrm{c}}} + r_{\mathrm{d}}\Theta\left(S_{\mathrm{c}}^{\mathrm{d}} - S_{\mathrm{c}}\right)\right)\right]. \tag{14}$$

The equation arises from setting $P_{\mathrm{g}}(i,t) = \frac{1}{2}$ in Equation (13) and solving for S_{o}. Here, the max function ensures that the oxygen concentration is non-negative at the growth threshold. For the parameter values in Table 1, $f_{\mathrm{th}}(S_{\mathrm{c}})$ is zero for $S_{\mathrm{c}} < S_{\mathrm{c}}^{\mathrm{d}}$ (see the inset of Figure 4). This is due to the dominance of the rate of lysis in this range of concentrations (see the inset in Figure 3), which makes growth essentially impossible. Increasing S_{c} leads to an increase in $f_{\mathrm{th}}(S_{\mathrm{c}})$ until a maximum value is reached:

$$S_{\mathrm{o}}^{\mathrm{u}} = \frac{r_{\mathrm{g}}}{a_{\mathrm{o}}}\left(1 - \sqrt{\frac{K_{\mathrm{g}}a_{\mathrm{c}}}{r_{\mathrm{g}}}}\right)^2, \tag{15}$$

for a nutrient concentration

$$S_{\mathrm{c}}^{*} = K_{\mathrm{g}}\left(\sqrt{\frac{r_{\mathrm{g}}}{K_{\mathrm{g}}a_{\mathrm{c}}}} - 1\right). \tag{16}$$

This expression is valid when $S_{\mathrm{c}}^{\mathrm{d}} < S_{\mathrm{c}}^{*}$, which is indeed the case for the values $S_{\mathrm{c}}^{*} = 1.065$ and $S_{\mathrm{c}}^{\mathrm{d}} = 0.0086$ mmol L^{-1} obtained for the model parameters in Table 1. The prediction of a peak in $f_{\mathrm{th}}(S_{\mathrm{c}})$ implies that the tolerance of cell growth to oxygen is maximal for intermediate values of the nutrient concentration. For $S_{\mathrm{c}} < S_{\mathrm{c}}^{*}$, growth becomes possible for a higher concentration of oxygen when increasing the nutrient concentration. Increasing the nutrient concentration beyond S_{c}^{*}, however, leads to a decreasing tolerance to oxygen due to the monotonic increase in the lysis rate with S_{c} compared to the growth rate that is limited in our model by the cell uptake capability (compare the curves for λ_{g} and λ_{l} in Figure 3). In fact, growth becomes unlikely (i.e., $P_{\mathrm{g}} < \frac{1}{2}$) for any concentration of oxygen if the nutrient concentration is above the following value:

$$S_{\mathrm{c}}^{\mathrm{u}} = \frac{r_{\mathrm{g}}}{a_{\mathrm{c}}} - K_{\mathrm{g}}. \tag{17}$$

In particular, $S_{\mathrm{c}}^{\mathrm{u}} = 39.97$ mmol L^{-1} for the parameters given in Table 1 (see Figure 3).

To summarize, the analysis of the behaviour of one cell predicts the existence of an optimal nutrient concentration for which the effective growth rate is maximized and thus increases the survival potential of the population in higher oxygen conditions. As a consequence, our analysis suggests that lower nutrient media may increase the tolerance of *C. jejuni* to higher oxygen conditions. This result may serve as a logical argument for a possible connection between *C. jejuni* being observed to grow better in lower nutrient media and its oxygen susceptibility [57,79].

The analysis of the behaviour of a single cell also reveals the expected dependence of the probability of growth on the parameters of the vital dynamics of the model. The value of the nutrient concentration S_{c}^{*} for which the tolerance to oxygen is maximal increases with the rate of growth, r_{g}, and decreases with the growth half saturation coefficient, K_{g}, and nutrient-induced lysis rate, a_{c}. The maximally tolerated oxygen concentration, $S_{\mathrm{o}}^{\mathrm{u}}$, and maximal nutrient concentration for which growth is likely to occur, $S_{\mathrm{c}}^{\mathrm{u}}$, exhibit similar trends with r_{g}, K_{g}, and a_{c}. In addition, $S_{\mathrm{o}}^{\mathrm{u}}$ decreases with the oxygen-related lysis rate, a_{o}. As intuitively expected, these trends suggest that the overall chances of cell growth increase with the rate of growth and decrease with the rates of lysis. The decrease with the half-saturation K_{g} is perhaps less intuitive but also makes sense since larger values of K_{g} induce a slower increase in the total growth rate, λ_{g}, with the nutrient concentration (see Equation (2)).

3.2. Collective Behaviour–Biofilm Formation

Here, we present results on the collective behaviour of cells by means of numerical simulations performed to study the effect of substrate concentrations and the diffusion of chemicals on biofilm formation. Numerical simulations are run on a rectangular environment with $L \times H$ patches, where $L = 20$ and $H = 50$. The linear size of each patch is set to $\delta = 5$ µm so that the simulation space is a rectangle with an area of 100×250 µm^2. All numerical simulations begin with a single triggering cell located at a randomly chosen patch, i^*, at the bottom of the system; the rest of the patches are occupied by fluid. The oxygen and carbon source concentrations are kept constant throughout the entire simulation at the upper horizontal boundary of the system. Such constant concentrations are denoted as S_o^H and S_c^H to indicate the fact that they correspond to patches at a height H. We assume that the concentration of chemical compounds is initially homogeneous in the system, i.e., concentrations are set to the values S_o^H and S_c^H at all the patches in the system. Following this, we shall refer to S_o^H and S_c^H as initial chemical concentrations.

3.2.1. Effect of Supplied Oxygen and Nutrient Concentrations

The numerical simulations presented in this section consider six different conditions in terms of the supplied chemical compound concentrations, S_c^H and S_o^H, that cover the regimes of likely and unlikely growth predicted for a single cell (see the circles in Figure 4).

More explicitly, simulations were run for two concentrations of oxygen: $S_\mathrm{o}^\mathrm{H} = 0.188$ and 0.26 mmol L^{-1}, corresponding to microaerobic and aerobic conditions in [79], respectively (approximate values from [79] were converted from ppm to mmol L^{-1} units). For each value of S_o^H, we explored the effect of three values of the supplied nutrient concentration, $S_\mathrm{c}^\mathrm{H} = 6.5$, 13, and 26 mmol L^{-1}. In particular, S_c^H =13 mmol L^{-1} corresponds to the sum of measured concentrations of aspartate, glutamate, serine, and proline in MHB in the experiments of Ref. [45]. The simulations presented in this section ran until the biofilm reached the upper horizontal boundary of the simulation rectangle, the cell population was extinct, or the simulation time reached the maximum time, which was set to 72 h. The diffusion constant in patches occupied by the biofilm (i.e., either in C or E-state) is set to $D_\mathrm{B} = 9 \times 10^{-11}$ m^2/s, which is 10 times smaller than the diffusion in the liquid (see Table 1 and Equation (7)). We observed three possible outcomes for a given stochastic realisation: (i) the biofilm may not start spreading; (ii) the biofilm may start spreading but the population of live cells becomes extinct before they invade the system in the vertical direction; and (iii) the biofilm may invade the system by reaching the upper boundary of the simulation rectangle at height H.

Biofilms do not start spreading (outcome (i)) if the triggering cell undergoes lysis or deactivation before duplicating. This occurs with probability $1 - P_\mathrm{g}(i*, t)$, where $P_\mathrm{g}(i*, t)$ is the probability that the triggering cell duplicates (see Equation (11)). In the numerical simulations, $P_\mathrm{g}(i*, t)$ is calculated as the fraction of times (out of 100) the triggering cell located at the bottom of the system duplicates before undergoing lysis or deactivation. Figure 5 shows analytical (dashed line) and numerical estimates (squares) of the probability that the biofilm starts growing, as a function of the supplied nutrient concentration, S_c^H, for the oxygen concentration $S_\mathrm{o}^\mathrm{H} = 0.3$ mmol L^{-1}. The peak of the probability suggests that biofilm formation is more likely for intermediate values of S_c^H ($S_\mathrm{c}^\mathrm{H} = 3$ mmol h^{-1} in the example of Figure 5). Indeed, at very low values of S_c^H, deactivation can occur (for $S_\mathrm{c}^\mathrm{H} < S_\mathrm{c}^\mathrm{d}$) and the rate of growth is small (see Figure 3). Growth is also hindered for high enough values of S_c^H due to a relative dominance of lysis.

When biofilms form, they can survive and invade the system to reach the upper boundary with probability P_inv. This probability is reminiscent of the probability of an epidemic in a lattice which was mapped to percolation [80,81]. By definition, $P_\mathrm{inv} \leq P_\mathrm{g}$, since invasion requires the duplication of the triggering cell and sustained growth of the population of live cells afterwards. For the given S_o^H, however, P_inv depends on S_c^H in a similar way as P_g in the sense that it displays a peak at intermediate values of S_c^H (see the crosses in Figure 5). The maximum value of P_inv, however, is located at a higher value of S_c^H

than that of P_g. In other words, the optimal nutrient concentration for biofilm invasion is higher than the nutrient concentration that optimizes the effective growth rate of individual cells. This is qualitatively expected since the local nutrient concentration within a biofilm is smaller than S_c^H due to the lower value of the diffusion constant in the biofilm compared to that in the fluid and nutrient consumed by the cells.

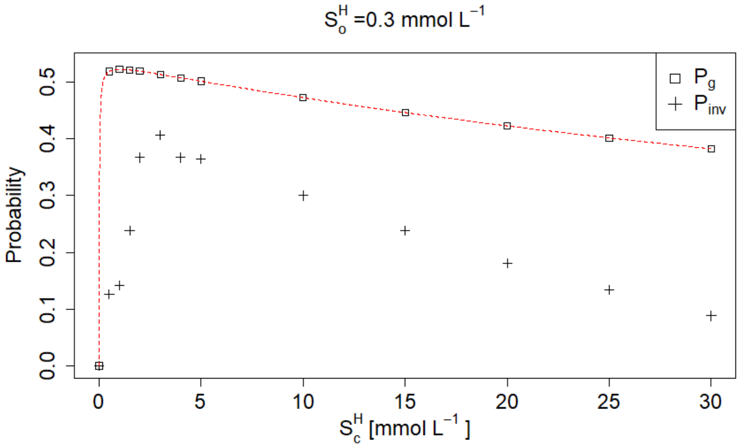

Figure 5. Probability P_{inv} that a triggering cell in high oxygen conditions S_o^H = 0.3 mmol h^{-1} leads to an invasive biofilm (crosses) compared to probability of growth of a single invading cell, $P_g(i,t)$ (squares for numerical simulations and dashed line for analytical results). Crosses indicate the survival probability of a triggering cell colony within 5 h simulations (fraction of runs out of 100 that reach the upper boundary of the system).

The diminished concentration of chemical compounds in patches occupied by the cells and ECM has important consequences for the collective behaviour of invading biofilms. In particular, this may lead to large biofilm invasions in conditions that are considered unfavourable for the growth of individual cells. In order to quantify these effects, we consider the mean number of live cells at a given time, defined as $\overline{n_C} = \sum_t n_C(t)/T$ for each invading biofilm. Here, T is the number of time steps (i.e., vital dynamics events) in a realisation and $n_C(t)$ is the number of live cells as a function of time. Figure 6 shows that histograms for $\overline{n_C}$ are bimodal, indicating a clear distinction between the situations when the colony does not invade (peak at low values of $\overline{n_C}$) and those in which the biofilm grows and spans the system. For any of the two oxygen levels considered in Figure 6, the peak of histograms at low $\overline{n_C}$ increases with S_c^H, meaning that invasion becomes more unlikely as S_c^H increases (i.e., P_{inv} decreases with S_c^H). On the other hand, the location of the peak on the right of the histograms moves to higher values of $\overline{n_C}$ as S_c^H increases. This implies that biofilm invasion becomes increasingly unlikely at higher nutrient concentrations but those biofilms that manage to span the system at high nutrient concentrations contain (on average) more live cells at a given time than those spanning at lower nutrient concentrations. This can be qualitatively explained in terms of the phase diagram in Figure 4 as a shelter effect induced by the biofilm. Indeed, the growth of individual cells will be unlikely at high nutrient concentrations (e.g., they are at the point (1) in Figure 4). In spite of that, if cells start duplicating and form a large enough biofilm, the chemical concentrations will decrease for some cells and their chances to duplicate increase (see the green arrow from point (1) in Figure 4).

The relative frequency of growth events in invasive biofilms takes values that are marginally above one half for all values of supplied nutrient and oxygen concentrations considered (see Figure 7). For all considered nutrient concentrations, increasing the level of oxygen significantly increased the frequency of lysis and decreased the frequency of deactivation in such a way that the frequency of growth remained essentially unaffected. As a result, nearly equivalent numbers of live cells were observed to reside within the colonies stemming from a single invading cell for both the low and high oxygen case, and a higher density of the biofilms was obtained in the aerobic conditions (due to an increase in the release of extracellular material in the lytic process).

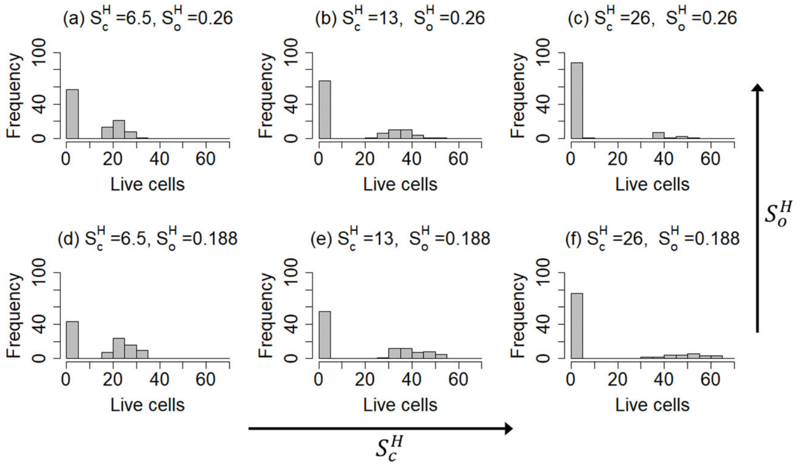

Figure 6. Histograms for the mean live cell counts, $\overline{n_C}$, for the combinations of chemical concentrations indicated by the red dots in Figure 4. The chemical concentration units are [mmol L^{-1}].

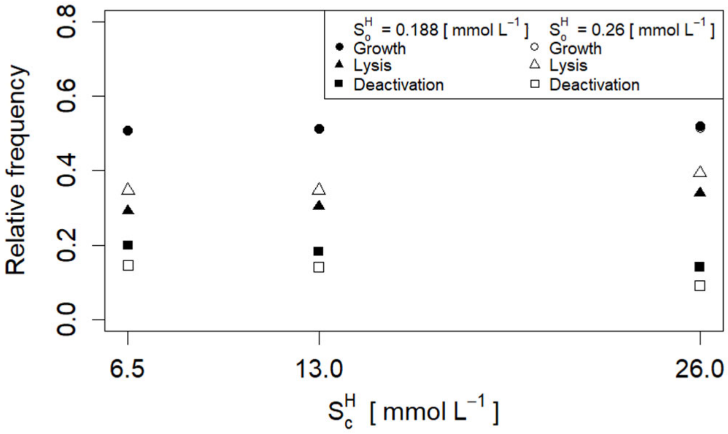

Figure 7. Relative frequencies of (●, ○) growth, (▲, △) lysis, and (■, □) deactivation events for invasive biofilms with different initial chemical concentrations S_c^H and S_o^H. The filled shapes represent lower oxygen conditions, where S_o^H = 0.188 mmol L^{-1}, and empty shapes represent cases where S_o^H = 0.26 mmol L^{-1}. Note that empty circles for aerobic conditions are not visible since they coincide with filled circles for microaerobic conditions for the set of parameters specified by Table 1.

It should be stressed that our simulations only focused on microcolonies, i.e., single cells invading the surface. In reality, there will be many cells invading the surface at the same time. Our results predict that the number of the cells in each of the invasive microcolonies could be equivalent in aerobic and microaerobic conditions, but at the same time, the invasion probability for each cell colonizing the surface is lower in higher oxygen conditions. This leads to the prediction of overall lower biofilm formation in aerobic conditions for the parameters specified in the model. This result is supported by experimental observations obtained by Teh et al., where it was observed that for eight different strains of *C. jejuni*, biofilm formation in MHB was equivalent or lower in aerobic conditions compared to microaerobic conditions [79]. On the other hand, the same study reported equivalent biofilm formation in Brucella broth under aerobic and microaerobic cultivation. It was suggested in the study that this could be due to a lower dissolved oxygen content in Brucella broth exposed to aerobic conditions when compared to MHB.

One can regard the relative frequency of growth events as a numerical estimate for the growth probability P_g introduced above. The fact that the relative frequency of growth events is slightly larger than 0.5 for invasive biofilms agrees with the requirement $P_g > \frac{1}{2}$ for cell growth to be likely.

At the level of individual cells, the considered values of S_c^H and S_o^H cover conditions of likely and unlikely growth (see circles in Figure 4). In spite of that, invasive biofilms are not very sensitive to the specific values of S_c^H and S_o^H. This suggests that biofilm formation leads to a self-organized state in which live cells are effectively near the $P_g = \frac{1}{2}$ threshold line in Figure 4 that separates the regimes of likely and unlikely growth.

The morphology of invasive biofilms depends on the supplied chemical concentrations. For lower nutrient concentrations, invasive biofilms describe ramified patterns with lower density (compare the panels in Figure 8a,b with Figure 8c). Increasing the supply of nutrients increases the frequency of lysis events and decreases the frequency of deactivation events. As a result, as the amount of the ECM increases, biofilms become denser (Figure 8c). At low fixed values of S_c^H, increasing the supply of oxygen, S_o^H, has a similar effect as that observed when increasing S_c^H at constant S_o^H (compare the left and right panel in Figure 8a).

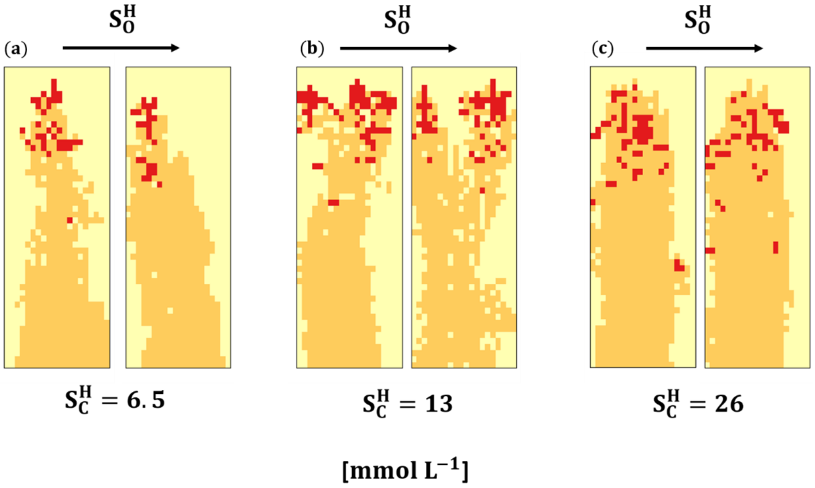

Figure 8. Structure of invasive biofilms for nutrient concentrations (**a**) S_c^H = 6.5 mmol h^{-1}, (**b**) S_c^H = 13 mmol h^{-1}, and (**c**) S_c^H = 26 mmol h^{-1}. The left and right panels for each value of S_c^H concentration correspond to low and high oxygen conditions, S_o^H = 0.188 mmol h^{-1} and S_o^H = 0.26 mmol h^{-1}, respectively. Red patches represent live cells and orange patches are occupied by ECM material. All patterns correspond to the time at which biofilms span the system vertically.

Each pattern in Figure 8 corresponds to the realisation in which the largest biofilm size out of 100 trials was obtained for the given set of parameters. Figure 9a shows that on average, for those biofilms that managed to invade the system, the biofilm size (number of patches occupied by cells or ECM) was found to increase by 5–9% in aerobic conditions compared to microaerobic conditions for lower nutrient concentrations (i.e., S_c^H = 6.5 and S_c^H = 13 mmol h^{-1}), and was equivalent for the higher nutrient concentration (S_c^H = 26 mmol h^{-1}). Interestingly, while a similar pattern was observed for biofilm density (Figure 9b), this was not true for all realisations, as the panel in Figure 8b shows (note a higher number of pores within the biofilm on the right panel in Figure 8b, compared to the left panel).

The specific concentrations of supplied chemicals do not only influence the morphology of biofilms but also affect the location of live cells. For relatively low values of S_c^H and S_o^H, live cells are mostly observed at the top of the biofilm where nutrients are more abundant (see Figure 8a,b). In contrast, for high levels of oxygen and nutrients, live cells are observed in deeper regions of the biofilm where the local concentrations are low enough for cell growth to be likely (Figure 8c). In such cases, the shelter provided by the biofilm is crucial for a population of live cells to exist.

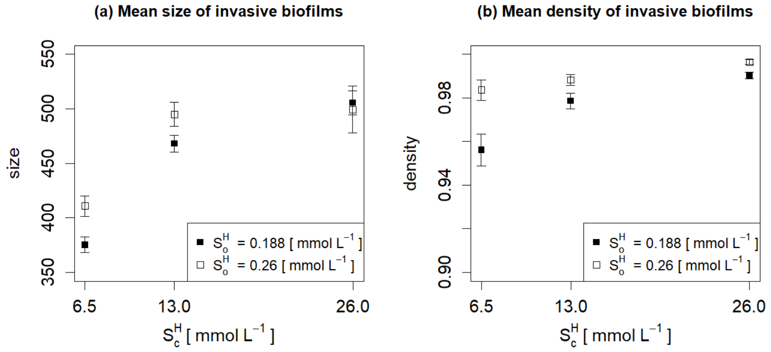

Figure 9. Average size (**a**) and density (**b**) of invasive biofilms. The error bars represent the standard error of the mean.

3.2.2. Effect of the Diffusion Coefficient in the Biofilm

In order to investigate the influence of the diffusion of chemical compounds in the biofilm, we ran simulations for a diffusion constant $D_B = 9 \times 10^{-10}$ m^2/s and compared with the results obtained in the previous section, where we set $D_B = 9 \times 10^{-11}$ m^2/s. As in for $D_B = 9 \times 10^{-11}$ m^2/s, we observed a significant depletion of nutrients in the lower sections of biofilms (Figure 8); so, we decided to see how the model behaved when the diffusion constant was increased.

In the case when chemical concentrations in the media are low enough, the increase in the diffusion coefficient was found to decrease the probability of invasion, P_{inv} (from 0.57 to 0.39), in agreement with predictions in Figure 4. However, for successful invasions, the mean number of live cells at a given time, $\overline{n_C}$, was found to increase by more than five-fold (from 24 to 123). In particular, more cells were observed at deeper regions of the biofilm for high diffusion which allows the concentrations of the nutrient within the biofilm to be higher compared to cases with lower diffusion (compare the patterns in Figure 10a,b).

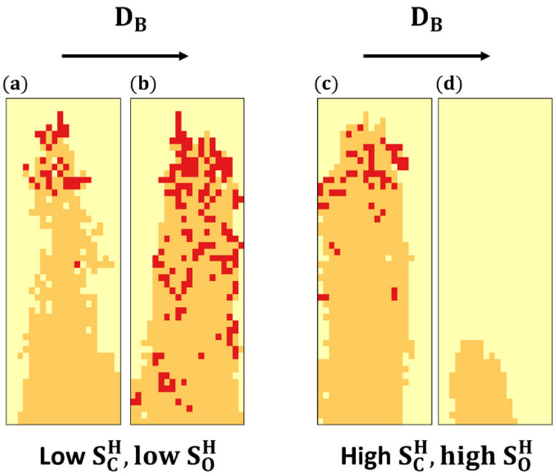

Figure 10. Effect of increasing the diffusion constant D_B of nutrient and oxygen within biofilms. Panels (**a**,**b**) correspond to $D_B = 9 \times 10^{-11}$ m^2/h and $D_B = 9 \times 10^{-10}$ m^2/h, respectively, for low supply of chemical compounds (S_c^H = 6.5 mmol h^{-1} and S_o^H = 0.188 mmol h^{-1}). Panels (**c**,**d**) show a similar arrangement for high supply of chemical compounds (S_c^H = 26 mmol h^{-1} and S_o^H = 0.26 mmol h^{-1}). In all panels the realisations for which the maximum biofilm size was achieved were chosen.

The effects of enhanced diffusion can be opposite in the case when the supply of nutrients and oxygen is high. Indeed, one observes high levels of nutrient and oxygen deeper inside the biofilm and this has a detrimental effect on growth due to high lysis rates. This is illustrated in Figure 10 where biofilms can invade if diffusion is low (panel (c)) but the invasion is unlikely for higher diffusion (see a non-invasive biofilm consisting of just ECM in panel (d)).

4. Conclusions

The model presented here is an individual-based, stochastic cellular automaton, in which events such as cell division and death are governed by a Poisson process with mean local event rates affected by changes in concentrations of carbon sources and oxygen. The results obtained from our analysis can be summarized as follows:

- The analysis of the behaviour of one cell predicts the existence of the optimal nutrient concentration for which the effective growth rate is maximized and thus it increases the survival potential of the population in higher oxygen conditions. In turn, this suggests that lower nutrient media may increase the tolerance of *C. jejuni* to higher oxygen conditions.
- The development of a biofilm, through decreasing local compound concentrations within its boundaries, may push the population towards the regime in which the effective growth rate is positive.
- The model predicts that the survival probability of individual cells placed on a surface decreases when nutrient or oxygen levels are raised. The expected number of live cells in situations when the cell is successful in establishing a colony, however, tend to be lower in the lower nutrient conditions. There appears to be a trade-off, where on the one hand, increasing nutrient conditions may be detrimental to individual cells, but at the same time it may bring benefit to the whole population.
- Our results suggest that the lower biofilm formation observed in aerobic conditions in Mueller Hinton Broth compared to cultivation in microaerobic conditions may be due to the lower surface invasion probability of individual cells, and that those cells which manage to invade may generate microcolonies of an equivalent size in aerobic and microaerobic conditions.

Our analysis focused on the comparison of the patterns found in the experimental observations to those generated by the model. It should be noted, however, that the model presented here is very versatile and it is possible that additional interesting predictions may be obtained with this or an extended model in the future.

The model could be improved by increasing the number of dimensions to three or increasing the size of the simulation space to study more mature biofilms. Additionally, extending our analysis to include biofilm growth initiated by multiple triggering cells, rather than just one as considered here, could reveal different biofilm morphologies depending on the model parameters [18,22,61,82]. Moreover, incorporating a metabolic network reconstruction, similar to what has been successfully conducted for *Escherichia coli* [20], could further refine the model. Once enough information about *C. jejuni* metabolism is revealed, additional mechanisms such as the release of metabolic products could be incorporated into our model and the effect of these mechanisms on the biofilm population could be assessed [16].

Author Contributions: Conceptualization, P.A.D., G.A.D., N.J.C.S., K.J.F. and F.J.P.-R.; methodology, P.A.D. and F.J.P.-R.; software, P.A.D.; validation, P.A.D. and F.J.P.-R.; formal analysis, P.A.D. and F.J.P.-R.; investigation, P.A.D. and F.J.P.-R.; writing—original draft preparation, P.A.D. and F.J.P.-R.; writing—review and editing, P.A.D., G.A.D., N.J.C.S., K.J.F. and F.J.P.-R.; project administration, G.A.D. and F.J.P.-R.; funding acquisition, G.A.D. and F.J.P.-R. All authors have read and agreed to the published version of the manuscript.

Funding: This work was supported by a scholarship grant from the School of Natural and Computing Sciences at the University of Aberdeen and the Faculty of Health Sciences at Curtin University. We also thank Food Standards Scotland (Contracts S14054 and FSS00017) for funding components of this study.

Institutional Review Board Statement: Not applicable.

Informed Consent Statement: Not applicable.

Data Availability Statement: The original contributions presented in the study are included in the article, further inquiries can be directed to the corresponding author/s. The code used to run the simulations can be found at https://github.com/fjpreche/StochasticBiofilm (accessed on 25 June 2024).

Conflicts of Interest: The authors declare no conflict of interest.

Appendix A. Algorithm for Vital Cell Dynamics

We assume that vital transition events define a Poisson point process such that, if the system reached a configuration field $\{\sigma(i,t)\}$ after a cell transition at time t, it would remain in such a state during a period of time Δt with probability $e^{-\Lambda(t)\Delta t}$. Here,

$$\Lambda(t) = \sum_{i \in \mathcal{B}(t)} \sum_{k \in \mathcal{E}} \lambda_k(i,t), \tag{A1}$$

is the decay rate of the state $\{\sigma(i,t)\}$ accounting for all the possible transitions, $\mathcal{E} = \{g,l,d\}$, of the patches occupied by cells, $\mathcal{B}(t) = \{i | \sigma(i,t) = C\}$. Within this formulation, the probability that we have to wait a time Δt between two consecutive cell transitions is $1 - e^{-\Lambda(t)\Delta t}$. In practice, the time Δt until the next cell event is calculated as follows:

$$\Delta t = -\frac{\ln(1-u)}{\Lambda(t)}\,, \tag{A2}$$

where u is a uniformly distributed random number in $[0,\ 1]$. A patch i occupied by a cell at time t is selected to undergo a transition $k \in \mathcal{E}$ after time Δt with probability $\Lambda(t)^{-1}\lambda_k(i,t)$.

Appendix B. Redistribution of Biofilm Mass after Growth Events

The path for the redistribution of biomass after a growth event is defined by first selecting an endpoint at random at the interface between the colony holding site i and the liquid medium (e.g., see the patch indicated by '×' in Figure 1). The distances in vertical and horizontal directions from the site at which duplication occurred to the endpoint are recorded. Then, randomly ordered, directed steps in the vertical and horizontal directions are applied, during which the surplus mass is pushed to the neighbouring site on the path, displacing what is already there to the next step of the path. The path in our algorithm is "directed", as the only movement allowed is that which shortens the distance to the endpoint. In other words, if the endpoint lies on the upper left side to the location where growth occurred, the only steps taken will be to the left and upwards, in randomized order. This shortens the algorithm substantially compared to a regular random path, especially for growth within large colonies. The algorithm ends once a site occupied by fluid is reached, either through reaching the endpoint of the path or by reaching a fluid site along the way, for example a pore or a channel within the biofilm matrix. This mass redistribution algorithm is reminiscent of the one proposed in [61], albeit the latter chose the end point of the path by calculating the shortest distance from the growth location to the biofilm surface, rather than randomly. In our model, as we allowed for the algorithm ending when encountering an empty space, we left the choice of the biofilm–liquid interface endpoint as random. This was performed, as in our model, choosing the shortest distance to the biofilm interface would not necessarily mean choosing the path of less resistance, as there may be pores along the way whose filling would offer less resistance.

In reality, cells would reorient themselves before moving further, provided that there is enough space to allow it. However, previously reported biofilm simulations, which took into account the reorienting of cells, have revealed that cells at the periphery may also be effectively pushed as a result of cell replications inside the biofilm [83], which motivated our simplified version of the biomass distribution.

References

1. Rumbaugh, K.P.; Sauer, K. Biofilm Dispersion. *Nat. Rev. Microbiol.* **2020**, *18*, 571–586. [CrossRef] [PubMed]
2. Marshall, K.C. Planktonic versus Sessile Life of Prokaryotes. In *The Prokaryotes: Prokaryotic Communities and Ecophysiology*; Springer: Berlin/Heidelberg, Germany, 2013; pp. 191–201. [CrossRef]
3. Flemming, H.C.; Wingender, J.; Szewzyk, U.; Steinberg, P.; Rice, S.A.; Kjelleberg, S. Biofilms: An Emergent Form of Bacterial Life. *Nat. Rev. Microbiol.* **2016**, *14*, 563–575. [CrossRef] [PubMed]
4. Davey, M.E.; O'toole, G.A. Microbial Biofilms: From Ecology to Molecular Genetics. *Microbiol. Mol. Biol. Rev.* **2000**, *64*, 847–867. [CrossRef] [PubMed]
5. Hall-Stoodley, L.; Costerton, J.W.; Stoodley, P. Bacterial Biofilms: From the Natural Environment to Infectious Diseases. *Nat. Rev. Microbiol.* **2004**, *2*, 95–108. [CrossRef] [PubMed]
6. Lewenza, S. Extracellular DNA-Induced Antimicrobial Peptide Resistance Mechanisms in Pseudomonas Aeruginosa. *Front. Microbiol.* **2013**, *4*, 21. [CrossRef] [PubMed]
7. Dincer, S.; Uslu, F.M.; Delik, A. Antibiotic Resistance in Biofilm. In *Bacterial Biofilms*; Dincer, S., Özdenefe, M.S., Arkut, A., Eds.; IntechOpen: Rijeka, Croatia, 2020; ISBN 978-1-78985-900-3.
8. Lewis, K. *Multidrug Tolerance of Biofilms and Persister Cells BT—Bacterial Biofilms*; Romeo, T., Ed.; Springer: Berlin/Heidelberg, Germany, 2008; pp. 107–131. ISBN 978-3-540-75418-3.
9. Wang, H.; Li, Y.; Yang, H.; Lin, K.A.; Shao, T.; Hope, J. Biofilms Controlling in Industrial Cooling Water Systems: A Mini-Review of Strategies and Best Practices. *ACS Appl. Bio Mater.* **2023**, *6*, 3213–3220. [CrossRef] [PubMed]
10. Carrel, M.; Morales, V.L.; Beltran, M.A.; Derlon, N.; Kaufmann, R.; Morgenroth, E.; Holzner, M. Biofilms in 3D Porous Media: Delineating the Influence of the Pore Network Geometry, Flow and Mass Transfer on Biofilm Development. *Water Res.* **2018**, *134*, 280–291. [CrossRef]
11. Percival, S.; Knottenbelt, D.; Cochrane, C. (Eds.) *Biofilms and Veterinary Medicine*; Springer Series on Biofilms; Springer: Berlin/Heidelberg, Germany, 2011; Volume 6, ISBN 978-3-642-21288-8.
12. Phalak, P.; Chen, J.; Carlson, R.P.; Henson, M.A. Metabolic Modeling of a Chronic Wound Biofilm Consortium Predicts Spatial Partitioning of Bacterial Species. *BMC Syst. Biol.* **2016**, *10*, 90. [CrossRef] [PubMed]
13. Simões, M.; Simões, L.C.; Vieira, M.J. A Review of Current and Emergent Biofilm Control Strategies. *LWT—Food Sci. Technol.* **2010**, *43*, 573–583. [CrossRef]
14. Liu, X.; Yao, H.; Zhao, X.; Ge, C. Biofilm Formation and Control of Foodborne Pathogenic Bacteria. *Molecules* **2023**, *28*, 2432. [CrossRef]
15. Dzianach, P.A.; Dykes, G.A.; Strachan, N.J.C.; Forbes, K.J.; Pérez-Reche, F.J. Challenges of Biofilm Control and Utilization: Lessons from Mathematical Modelling. *J. R. Soc. Interface* **2019**, *16*, 20190042. [CrossRef]
16. Dzianach, P.A.; Pérez-Reche, F.J.; Strachan, N.J.C.; Forbes, K.J.; Dykes, G.A. The Use of Interdisciplinary Approaches to Understand the Biology of *Campylobacter jejuni*. *Microorganisms* **2022**, *10*, 2498. [CrossRef] [PubMed]
17. Wilkinson, D.J. Stochastic Modelling for Quantitative Description of Heterogeneous Biological Systems. *Nat. Rev. Genet.* **2009**, *10*, 122–133. [CrossRef] [PubMed]
18. Rodriguez, D.; Einarsson, B.; Carpio, A. Biofilm Growth on Rugose Surfaces. *Phys. Rev. E Stat. Nonlinear Soft Matter Phys.* **2012**, *86*, 061914. [CrossRef] [PubMed]
19. Lardon, L.A.; Merkey, B.V.; Martins, S.; Dötsch, A.; Picioreanu, C.; Kreft, J.U.; Smets, B.F. IDynoMiCS: Next-Generation Individual-Based Modelling of Biofilms. *Environ. Microbiol.* **2011**, *13*, 2416–2434. [CrossRef] [PubMed]
20. Tack, I.L.M.M.; Nimmegeers, P.; Akkermans, S.; Hashem, I.; Van Impe, J.F.M. Simulation of *Escherichia coli* Dynamics in Biofilms and Submerged Colonies with an Individual-Based Model Including Metabolic Network Information. *Front. Microbiol.* **2017**, *8*, 2509. [CrossRef] [PubMed]
21. Chanbless, J.D.; Hunt, S.M.; Stewart, P.S. A Three-Dimensional Computer Model of Four Hypothetical Mechanisms Protecting Biofilms from Antimicrobials. *Appl. Environ. Microbiol.* **2006**, *72*, 2005–2013. [CrossRef] [PubMed]
22. Xavier, J.B.; Picioreanu, C.; Van Loosdrecht, M.C.M. A Framework for Multidimensional Modelling of Activity and Structure of Multispecies Biofilms. *Environ. Microbiol.* **2005**, *7*, 1085–1103. [CrossRef]
23. Haas, C.N. Microbial Dose Response Modeling: Past, Present, and Future. *Environ. Sci. Technol.* **2015**, *49*, 1245–1259. [CrossRef]
24. Perez-Reche, F.J. Impact of Heterogeneity on Infection Probability: Insights from Single-Hit Dose-Response Models. *arXiv* **2024**, arXiv:2404.00822.
25. Chen, L.; Geys, H.; Cawthraw, S.; Havelaar, A.; Teunis, P. Dose Response for Infectivity of Several Strains of *Campylobacter jejuni* in Chickens. *Risk Anal.* **2006**, *26*, 1613–1621. [CrossRef] [PubMed]
26. Teunis, P.F.M.; Nagelkerke, N.J.D.; Haas, C.N. Dose Response Models for Infectious Gastroenteritis. *Risk Anal.* **1999**, *19*, 1251–1260. [CrossRef] [PubMed]
27. Teunis, P.F.M.; Ogden, I.D.; Strachan, N.J.C. Hierarchical Dose Response of *E. coli* O157:H7 from Human Outbreaks Incorporating Heterogeneity in Exposure. *Epidemiol. Infect.* **2008**, *136*, 761–770. [CrossRef] [PubMed]
28. Teunis, P.F.M.; Kasuga, F.; Fazil, A.; Ogden, I.D.; Rotariu, O.; Strachan, N.J.C. Dose–Response Modeling of Salmonella Using Outbreak Data. *Int. J. Food Microbiol.* **2010**, *144*, 243–249. [CrossRef] [PubMed]

29. Teunis, P.F.; Marinović, A.B.; Tribble, D.R.; Porter, C.K.; Swart, A. Acute Illness from *Campylobacter jejuni* May Require High Doses While Infection Occurs at Low Doses. *Epidemics* **2018**, *24*, 1–20. [CrossRef] [PubMed]
30. Campylobacter. Available online: https://www.who.int/news-room/fact-sheets/detail/campylobacter (accessed on 25 June 2024).
31. O'Brien, S.J. The Consequences of Campylobacter Infection. *Curr. Opin. Gastroenterol.* **2017**, *33*, 14–20. [CrossRef] [PubMed]
32. Davis, L.; DiRita, V. Growth and Laboratory Maintenance of *Campylobacter jejuni*. *Curr. Protoc. Microbiol.* **2008**, *10*, 8A.1.1–8A.1.7. [CrossRef] [PubMed]
33. Hofreuter, D. Defining the Metabolic Requirements for the Growth and Colonization Apacity of *Campylobacter jejuni*. *Front. Cell. Infect. Microbiol.* **2014**, *4*, 137. [CrossRef] [PubMed]
34. Sulaeman, S.; Hernould, M.; Schaumann, A.; Coquet, L.; Bolla, J.-M.; Dé, E.; Tresse, O. Enhanced Adhesion of *Campylobacter jejuni* to Abiotic Surfaces Is Mediated by Membrane Proteins in Oxygen-Enriched Conditions. *PLoS ONE* **2012**, *7*, e46402. [CrossRef]
35. Wagenaar, J.A.; Newell, D.G.; Kalupahana, R.S.; Mughini-Gras, L. *Campylobacter*: Animal Reservoirs, Human Infections, and Options for Control. In *Zoonoses: Infections Affecting Humans and Animals*; Springer: Dordrecht, The Netherlands, 2023; pp. 267–293. [CrossRef]
36. Mughini Gras, L.; Smid, J.H.; Wagenaar, J.A.; de Boer, A.G.; Havelaar, A.H.; Friesema, I.H.M.; French, N.P.; Busani, L.; van Pelt, W. Risk Factors for Campylobacteriosis of Chicken, Ruminant, and Environmental Origin: A Combined Case-Control and Source Attribution Analysis. *PLoS ONE* **2012**, *7*, e42599. [CrossRef]
37. Cody, A.J.; Maiden, M.C.J.; Strachan, N.J.C.; McCarthy, N.D. A Systematic Review of Source Attribution of Human Campylobacteriosis Using Multilocus Sequence Typing. *Eurosurveillance* **2019**, *24*, 1800696. [CrossRef] [PubMed]
38. Pérez-Reche, F.J.; Rotariu, O.; Lopes, B.S.; Forbes, K.J.; Strachan, N.J.C. Mining Whole Genome Sequence Data to Efficiently Attribute Individuals to Source Populations. *Sci. Rep.* **2020**, *10*, 12124. [CrossRef] [PubMed]
39. Doyle, M.P.; Roman, D.J. Prevalence and Survival of *Campylobacter jejuni* in Unpasteurized Milk. *Appl. Environ. Microbiol.* **1982**, *44*, 1154–1158. [CrossRef] [PubMed]
40. Strachan, N.J.C.; Rotariu, O.; MacRae, M.; Sheppard, S.K.; Smith-Palmer, A.; Cowden, J.; Maiden, M.C.J.; Forbes, K.J. Operationalising Factors That Explain the Emergence of Infectious Diseases: A Case Study of the Human Campylobacteriosis Epidemic. *PLoS ONE* **2013**, *8*, e79331. [CrossRef] [PubMed]
41. Mulder, A.C.; Franz, E.; de Rijk, S.; Versluis, M.A.J.; Coipan, C.; Buij, R.; Müskens, G.; Koene, M.; Pijnacker, R.; Duim, B.; et al. Tracing the Animal Sources of Surface Water Contamination with *Campylobacter jejuni* and *Campylobacter coli*. *Water Res.* **2020**, *187*, 116421. [CrossRef]
42. Thépault, A.; Rose, V.; Queguiner, M.; Chemaly, M.; Rivoal, K. Dogs and Cats: Reservoirs for Highly Diverse *Campylobacter jejuni* and a Potential Source of Human Exposure. *Animals* **2020**, *10*, 838. [CrossRef] [PubMed]
43. Parsons, B.N.; Porter, C.J.; Ryvar, R.; Stavisky, J.; Williams, N.J.; Pinchbeck, G.L.; Birtles, R.J.; Christley, R.M.; German, A.J.; Radford, A.D.; et al. Prevalence of Campylobacter Spp. in a Cross-Sectional Study of Dogs Attending Veterinary Practices in the UK and Risk Indicators Associated with Shedding. *Vet. J.* **2010**, *184*, 66–70. [CrossRef] [PubMed]
44. Bronowski, C.; James, C.E.; Winstanley, C. Role of Environmental Survival in Transmission of *Campylobacter jejuni*. *FEMS Microbiol. Lett.* **2014**, *356*, 8–19. [CrossRef]
45. Teh, A.H.T.; Lee, S.M.; Dykes, G.A. Association of Some *Campylobacter jejuni* with *Pseudomonas aeruginosa* Biofilms Increases Attachment under Conditions Mimicking Those in the Environment. *PLoS ONE* **2019**, *14*, e0215275. [CrossRef]
46. Svensson, S.L.; Pryjma, M.; Gaynor, E.C. Flagella-Mediated Adhesion and Extracellular DNA Release Contribute to Biofilm Formation and Stress Tolerance of *Campylobacter jejuni*. *PLoS ONE* **2014**, *9*, e106063. [CrossRef]
47. Yoon, K.S.; Burnette, C.N.; Oscar, T.P. Development of Predictive Models for the Survival of *Campylobacter jejuni* (ATCC 43051) on Cooked Chicken Breast Patties and in Broth as a Function of Temperature. *J. Food Prot.* **2004**, *67*, 64–70. [CrossRef] [PubMed]
48. González, M.; Skandamis, P.N.; Hänninen, M.-L. A Modified Weibull Model for Describing the Survival of *Campylobacter jejuni* in Minced Chicken Meat. *Int. J. Food Microbiol.* **2009**, *136*, 52–58. [CrossRef] [PubMed]
49. McCarthy, Z.; Smith, B.; Fazil, A.; Wu, J.; Ryan, S.D.; Munther, D. PH Dependent *C. jejuni* Thermal Inactivation Models and Application to Poultry Scalding. *J. Food Eng.* **2018**, *223*, 1–9. [CrossRef]
50. Metris, A.; Reuter, M.; Gaskin, D.J.H.; Baranyi, J.; van Vliet, A.H.M. In Vivo and in Silico Determination of Essential Genes of *Campylobacter jejuni*. *BMC Genom.* **2011**, *12*, 535. [CrossRef] [PubMed]
51. de Vries, S.P.; Gupta, S.; Baig, A.; Wright, E.; Wedley, A.; Jensen, A.N.; Lora, L.L.; Humphrey, S.; Skovgård, H.; Macleod, K.; et al. Genome-Wide Fitness Analyses of the Foodborne Pathogen *Campylobacter jejuni* in In Vitro and In Vivo Models. *Sci. Rep.* **2017**, *7*, 1251. [CrossRef] [PubMed]
52. Giallourou, N.; Medlock, G.L.; Bolick, D.T.; Medeiros, P.H.Q.S.; Ledwaba, S.E.; Kolling, G.L.; Tung, K.; Guerry, P.; Swann, J.R.; Guerrant, R.L. A Novel Mouse Model of *Campylobacter jejuni* Enteropathy and Diarrhea. *PLoS Pathog.* **2018**, *14*, e1007083. [CrossRef] [PubMed]
53. Black, R.E.; Perlman, D.; Clements, M.L.; Levine, M.M.; Blaser, M.J. Human Volunteer Studies with *Campylobacter jejuni*. In *Campylobacter jejuni: Current Status and Future Trends*; Nachamkin, I., Blaser, M.J., Tompkins, L., Eds.; ASM Press: Washington, DC, USA, 1993; pp. 207–215.

54. Bacon, D.J.; Alm, R.A.; Burr, D.H.; Hu, L.; Kopecko, D.J.; Ewing, C.P.; Trust, T.J.; Guerry, P. Involvement of a Plasmid in Virulence of *Campylobacter jejuni* 81-176. *Infect. Immun.* **2000**, *68*, 4384–4390. [CrossRef]
55. Bereswill, S.; Fischer, A.; Plickert, R.; Haag, L.-M.; Otto, B.; Kühl, A.A.; Dashti, J.I.; Zautner, A.E.; Muñoz, M.; Loddenkemper, C.; et al. Novel Murine Infection Models Provide Deep Insights into the "Ménage à Trois" of *Campylobacter jejuni*, Microbiota and Host Innate Immunity. *PLoS ONE* **2011**, *6*, e20953. [CrossRef]
56. Teh, A.H.T.; Lee, S.M.; Dykes, G.A. The Influence of Prior Modes of Growth, Temperature, Medium, and Substrate Surface on Biofilm Formation by Antibiotic-Resistant *Campylobacter jejuni*. *Curr. Microbiol.* **2016**, *73*, 859–866. [CrossRef]
57. Reeser, R.J.; Medler, R.T.; Billington, S.J.; Jost, B.H.; Joens, L.A. Characterization of *Campylobacter jejuni* Biofilms under Defined Growth Conditions. *Appl. Environ. Microbiol.* **2007**, *73*, 1908–1913. [CrossRef]
58. Reuter, M.; Mallett, A.; Pearson, B.M.; Van Vliet, A.H.M. Biofilm Formation by *Campylobacter jejuni* Is Increased under Aerobic Conditions. *Appl. Environ. Microbiol.* **2010**, *76*, 2122–2128. [CrossRef] [PubMed]
59. Feng, J.; Ma, L.; Nie, J.; Konkel, M.E.; Lu, X. Environmental Stress-Induced Bacterial Lysis and Extracellular DNA Release Contribute to *Campylobacter jejuni* Biofilm Formation. *Appl. Environ. Microbiol.* **2018**, *84*, e02068-17. [CrossRef] [PubMed]
60. Ben-Jacob, E.; Schochet, O.; Tenenbaum, A.; Cohen, I.; Czirok, A.; Vicsek, T. Generic Modelling of Cooperative Growth Patterns in Bacterial Colonies. *Nature* **1994**, *368*, 46–49. [CrossRef] [PubMed]
61. Hermanowicz, S.W. A Simple 2D Biofilm Model Yields a Variety of Morphological Features. *Math. Biosci.* **2001**, *169*, 1–14. [CrossRef] [PubMed]
62. Wimpenny, J.W.T.; Colasanti, R. A Unifying Hypothesis for the Structure of Microbial Biofilms Based on Cellular Automaton Models. *FEMS Microbiol. Ecol.* **1997**, *22*, 1–16. [CrossRef]
63. Picioreanu, C.; Van Loosdrecht, M.C.M.; Heijnen, J.J. Mathematical Modeling of Biofilm Structure with a Hybrid Differential-Discrete Cellular Automaton Approach. *Biotechnol. Bioeng.* **1998**, *58*, 101–116. [CrossRef]
64. Eberl, H.J.; Parker, D.F.; Van Loosdrecht, M.C.M. A New Deterministic Spatio-Temporal Continuum Model for Biofilm Development. *Comput. Math. Methods Med.* **2000**, *3*, 161–175. [CrossRef]
65. Sen, P.N. Time-Dependent Diffusion Coefficient as a Probe of Geometry. *Concepts Magn. Reson. Part A Bridg. Educ. Res.* **2004**, *23*, 1–21. [CrossRef]
66. Xavier, J.B.; Picioreanu, C.; van Loosdrecht, M.C.M. A Modelling Study of the Activity and Structure of Biofilms in Biological Reactors. *Biofilms* **2004**, *1*, 377–391. [CrossRef]
67. Pérez-Reche, F.J.; Taraskin, S.N.; Otten, W.; Viana, M.P.; Costa, L.D.F.; Gilligan, C.A. Prominent Effect of Soil Network Heterogeneity on Microbial Invasion. *Phys. Rev. Lett.* **2012**, *109*, 098102. [CrossRef]
68. Pérez-Reche, F.J.; Ludlam, J.J.; Taraskin, S.N.; Gilligan, C.A. Synergy in Spreading Processes: From Exploitative to Explorative Foraging Strategies. *Phys. Rev. Lett.* **2011**, *106*, 218701. [CrossRef]
69. Gilligan, C.A.; van den Bosch, F. Epidemiological Models for Invasion and Persistence of Pathogens. *Annu. Rev. Phytopathol.* **2008**, *46*, 385–418. [CrossRef]
70. Guccione, E.; del Rocio Leon-Kempis, M.; Pearson, B.M.; Hitchin, E.; Mulholland, F.; van Diemen, P.M.; Stevens, M.P.; Kelly, D.J. Amino Acid-Dependent Growth of *Campylobacter jejuni*: Key Roles for Aspartase (AspA) under Microaerobic and Oxygen-Limited Conditions and Identification of AspB (Cj0762), Essential for Growth on Glutamate. *Mol. Microbiol.* **2008**, *69*, 77–93. [CrossRef] [PubMed]
71. Jansen, A.P.J. Kinetic Monte Carlo Algorithms. In *An Introduction to Kinetic Monte Carlo Simulations of Surface Reactions*; Beiglböck, W., Ehlers, J., Hepp, K., Weidenmüller, H., Eds.; Springer: Berlin/Heidelberg, Germany, 2012; pp. 37–71, ISBN 978-3-642-29488-4.
72. Duffy, L.L.; Dykes, G.A. The Ability of *Campylobacter jejuni* Cells to Attach to Stainless Steel Does Not Change as They Become Nonculturable. *Foodborne Pathog. Dis.* **2009**, *6*, 631–634. [CrossRef]
73. Stewart, P.S. Diffusion in Biofilms. *J. Bacteriol.* **2003**, *185*, 1485–1491. [CrossRef]
74. Smith, G.D. *Numerical Solution of Partial Differential Equations: Finite Difference Methods*, 3rd ed.; Oxford University Press: New York, NY, USA, 1985; ISBN 0-19-859641-3.
75. Mohammed, K.A.S.; Miles, R.J.; Halablab, M.A. The Pattern and Kinetics of Substrate Metabolism of *Campylobacter jejuni* and *Campylobacter coli*. *Lett. Appl. Microbiol.* **2004**, *39*, 261–266. [CrossRef] [PubMed]
76. Hazeleger, W.C.; Wouters, J.A.; Rombouts, F.M.; Abee, T. Physiological Activity of *Campylobacter jejuni* Far below the Minimal Growth Temperature. *Appl. Environ. Microbiol.* **1998**, *64*, 3917–3922. [CrossRef]
77. Schulze, K.L.; Lipe, R.S. Relationship between Substrate Concentration, Growth Rate, and Respiration Rate of *Escherichia coli* in Continuous Culture. *Arch. Mikrobiol.* **1964**, *48*, 1–20. [CrossRef]
78. Rollins, D.M.; Colwell, R.R. Viable but Nonculturable Stage of *Campylobacter jejuni* and Its Role in Survival in the Natural Aquatic Environment. *Appl. Environ. Microbiol.* **1986**, *52*, 531–538. [CrossRef]
79. Teh, A.H.T.; Lee, S.M.; Dykes, G.A. The Influence of Dissolved Oxygen Level and Medium on Biofilm Formation by *Campylobacter jejuni*. *Food Microbiol.* **2017**, *61*, 120–125. [CrossRef]
80. Pérez-Reche, F.J.; Taraskin, S.N.; da F. Costa, L.; Neri, F.M.; Gilligan, C.A. Complexity and Anisotropy in Host Morphology Make Populations Less Susceptible to Epidemic Outbreaks. *J. R. Soc. Interface* **2010**, *7*, 1083–1092. [CrossRef] [PubMed]
81. Grassberger, P. On the Critical Behavior of the General Epidemic Process and Dynamical Percolation. *Math. Biosci.* **1983**, *63*, 157–172. [CrossRef]

82. Flemming, H.C.; Wingender, J. The Biofilm Matrix. *Nat. Rev. Microbiol.* **2010**, *8*, 623–633. [CrossRef] [PubMed]
83. Yan, J.; Sharo, A.G.; Stone, H.A.; Wingreen, N.S.; Bassler, B.L. Vibrio Cholerae Biofilm Growth Program and Architecture Revealed by Single-Cell Live Imaging. *Proc. Natl. Acad. Sci. USA* **2016**, *113*, e5337–e5343. [CrossRef]